Surface & Coatings Technology 450 (2022) 128982

Contents lists available at ScienceDirect

Surface & Coatings Technology

journal homepage: www.elsevier.com/locate/surfcoat

Comparison between pilot and lab scale testing of aluminide coated and uncoated ferritic steels under oxy-fuel and coal/thistle co-firing conditions

M. Gutiérrez [a,*], A. Illana [b], A. Bahillo [c], M.J. Benito [c], G. García-Martín [b], F.J. Pérez [b], A. Agüero [a]

[a] Instituto Nacional de Técnica Aeroespacial (INTA), Ctra. Ajalvir Km 4, 28850 Torrejón de Ardoz, Madrid, Spain
[b] Surface Engineering and Nanostructured Materials Research Group, Universidad Complutense de Madrid, Avda. Complutense S/N, 28040 Madrid, Spain
[c] Department of Energy, Centro de Investigaciones Energéticas, Medioambientales y Tecnológicas (CIEMAT), Avda. Complutense 40, 28040 Madrid, Spain

ARTICLE INFO

Keywords:
High temperature corrosion
Oxy-fuel combustion
Biomass
Co-firing
Slurry coating
Pilot plant testing

ABSTRACT

The present study compares the biomass corrosion behavior of two diffusion aluminide coating obtained by slurry application, which were deposited on two low-chromium content steels, ferritic-martensitic P92 (8.7 wt% Cr) and ferritic T22 (2 wt% Cr). Their performance degradation was conducted under an oxy-fuel combustion environment for both coated and uncoated materials both under laboratory conditions and in a pilot plant burning thistle for 500 h. Exposures were carried out in the laboratory at two different temperatures, 600 °C and 650 °C, under a model atmosphere consisting of 60 % CO_2, 30 % H_2O, 8 % O_2, bal.% N_2 (in vol%), 500 vppm HCl and 2 vppm SO_2. The pilot plant used a mixed fuel of 60 wt% coal and 40 wt% thistle that was burnt and the samples were exposed to a temperature range of 600–620 °C. After testing, the results revealed that the aluminide-coated materials exhibited a very high resistance under both extreme scenarios, with a variable protective character related to their Al content. On the contrary, uncoated material exhibited severe degradation, in particular T22. Microstructural and morphological studies showed up similar corrosion patterns and products on coated and uncoated materials for both testing environments.

1. Introduction

A promising way to reduce CO_2 emissions and waste disposal problems is to partially or totally replace coal by biomass [1], which is one of the most abundant renewable resources and is considered as a carbon-neutral source [2]. For instance, it is estimated that using 1–10 % biomass co-firing in coal power plants could reduce the CO_2 emissions from 45 to 450 million tons per year by 2035 [3]. In addition, emissions of other greenhouse gases from coal burning, such as SO_2 and NO_x, are also reduced, thus also causing less environmental pollution [4].

However, the use of coal-biomass co-firing with only 10 % of biomass has two mainly disadvantages: (1) the levelized cost of electricity (LCOE) is significantly higher (nearly 8 %) than that of a pure coal-fired unit, due to the higher price of biomass relative to coal [4,5], and (2) the energy efficiency in the boiler may be reduced from 0.5 to 1 % [6], due to severe corrosion problems which result from biomass combustion. Indeed, current coal-biomass power plants are limited to a working temperature at a maximum of 540 °C (steam temperature) [7], thus obtaining efficiencies of 35–44 % (depending on the plant technology, size, quality and biomass feedstock) [3,8]. These corrosion issues are a consequence of the biomass chemical composition which is rich in heavy metals, sulfur and chlorine (Cl_2) [7,9,10], but above all, aggressive alkali chlorides (e.g. KCl or NaCl). These species are deposited on the boiler surface during the operation, not only initiating corrosion mechanisms due to the reaction with other metal chlorides ($FeCl_2$, $NiCl_2$, $CrCl_2$, etc.) which generate low-melting-point eutectic compounds [11], but also causing problems such as slagging and fouling which reduce heat transfer [3]. Therefore, current coal-biomass power plants have to use stainless steels and Ni base alloys for better corrosion resistance in critical components [12], increasing the capital expenditure (CAPEX).

Increasing efficiency is critical to further reduce greenhouse emissions, but this entails higher temperature operation which in turn results in increased corrosion rates and reduction of the materials lifetime. In parallel, in order to simplify CO_2 capture, the plants can operate under oxy-fuel combustion conditions, with pure oxygen instead of air so that NO_x emissions are avoided [13,14]. Hence, this evolution necessarily involves: (1) developing advanced alloys with additions of Al or/and Cr to improve oxidation and high-temperature corrosion resistance without

* Corresponding author.
E-mail addresses: gutierrezdom@inta.es (M. Gutiérrez), ailla01@ucm.es (A. Illana), alberto.bahillo@ciemat.es (A. Bahillo), mj.benito@ciemat.es (M.J. Benito), gusgarci@ucm.es (G. García-Martín), fjperez@ucm.es (F.J. Pérez), agueroba@inta.es (A. Agüero).

https://doi.org/10.1016/j.surfcoat.2022.128982
Received 9 August 2022; Received in revised form 5 October 2022; Accepted 15 October 2022
Available online 20 October 2022

Table 1
Composition (as given by the provider) of T22 and P92 steels (in wt%).

	Cr	W	Mo	Mn	Si	V	C	S	P	N	Ni	Al	B	Nb
T22	2.0	–	0.9	0.4	0.5	–	0.1	0.025	0.025	0.009	–	–	–	–
P92	8.7	1.65	0.38	0.49	0.21	0.18	0.12	0.002	0.014	0.053	0.17	0.01	0.003	0.06

reducing the creep strength [11], (2) using better austenitic steels or Ni-base alloys in spite of their higher costs [15], or (3) applying protective coatings on lower costs ferritic or ferritic-martensitic steels, since these raw materials have low oxidation resistance at those conditions [16,17].

Considering that there is interest in reducing the LCOE resulting from this hybrid technology, an excellent technical and economical solution is to use coatings on lower cost steels [11]. In fact, several studies have focused on coatings such as SiC or Al_2O_3 ceramic refractory linings and tiles, thermal spray coatings, weld overlays of Ni-base alloys (e.g. alloy 625) and aluminide diffusion coatings in order to allow longer operation times under combustion and/or oxy-combustion environments at 600–650 °C [18,19].

Adherent coatings applied by means of thermal spray techniques are a promising approach to improving the lifetime of the components and, thus, significantly increasing the thermal/electrical efficiency of power plants. Notwithstanding, thermal spray coatings exhibit a few intrinsic limitations, including the presence of porosity and relatively weak inter-splat bonding that lead to increased corrosion susceptibility [11]. For instance, the behavior of Ni-based coatings deposited by HVOF was studied by Hussain and collaborators [20,21]. Ni50Cr [20] and Ni20Cr [21] coatings applied on ferritic steels were exposed to 500 ppm HCl, 5 vol% O_2 (bal. N_2) with deposits of KCl at 700 °C for 250 h, and different deposits of NaCl, KCl, Na_2SO_4 and K_2SO_4 at 650 °C for 360 h in dry air, respectively, and the results showed that the chloride-rich salts progressed readily between the splat boundaries.

Other studied coatings are the durable weld overlays which exhibit very low porosity and have high resistance to corrosion and very strong adhesion due to the high-heat welding process, which results in the formation of a metallurgical bond with the base metal, essentially alloying the coating on the substrate at the interface. On the other hand, the surface of the weld overlay coatings is typically rough and uneven and can accelerate corrosion through easier sticking of slag, or produce lower coating thickness areas that concentrate heat flux. The weld overlays can only be applied in high thicknesses (~2–3 mm), which may increase the temperature drop across the layer. Indeed, the lower thermal conductivity of the weld overlay coatings due to their high thickness leads to an increase in the proportion of heat absorbed in the upper furnace and convection pass, resulting in a deviation from the design heat balance of the boiler, as well as the tendency of thermal fatigue cracking of the coated tubes [11].

Finally, A. Agüero et al. deposited aluminide coatings with 52 wt% Al and 4 wt% Cr on ferritic steels which showed excellent behavior in fire-side corrosion up to 650 °C. This low cost coating formulation is stable for >6 months under an oxy-fuel-coal combustion model atmosphere and also environmentally friendly [17]. This coating requires a 700 °C diffusion heat treatment after deposition of the Al slurry formulation, and through-thickness cracks develop within the coatings during cooling. These cracks are likely due to brittleness of the Fe_2Al_5 phase as well as mismatch of the thermal expansion coefficients of the different phases and the substrate but the cracks self-heal and do not become paths for the corrosive gases to reach the substrate. The same research group sought to avoid crack development by applying a heat treatment at higher temperatures promoting significantly faster Fe-Al interdiffusion thereby reducing the content of Al and Cr in the surface to 18-20 wt% and 4 wt%, respectively. This resulted in the formation of the less brittle and prone to crack intermetallic FeAl, but Kirkendall porosity was observed at the interface between the FeAl layer and the substrate. These aluminide coatings have been tested in an industrial pilot oxy-combustion boiler employing a mixture of biomass and coal as fuel for 480 h at 650 °C and no degradation was observed despite the presence of deposited ashes on the surface of the coating [22]. Moreover, Cr and Ni enriched aluminides have been studied in a preliminary test by A. Agüero et al. The Cr aluminide coating may represent an improvement over the pure aluminide coating as it does not exhibit cracks and degradation by diffusion is significantly slower. However, Ni aluminide coatings needed improvement in order to eliminate the possibility of internal oxidation likely related to the presence of P as a result of the Ni(P) electroless process [22].

There is a global inevitable and irreversible trend to gradually replace fossil fuels with renewable sources of energy to achieve sustainability and to reduce the negative environmental aspects associated with fossil fuels. Biomass co-firing can have a very influential role in contributing to achieve this target as it is a CO_2 neutral sustainable resource. Well-designed and reliable laboratory testing is therefore needed to evaluate the high temperature corrosion resistance of new material systems including coatings, under the very complex atmospheres resulting from biomass and biomass/coal mixtures in order to screen materials and to reduce the cost associated with in-plant testing. However, there is no general agreement regarding the methodology to carry out biomass corrosion. A laboratory test procedure based on data obtained from a thistle/coal-burning pilot plant employing oxy-combustion conditions, was established and the corresponding rig implemented. A model atmosphere was chosen on the basis of the composition of gases measured in the corresponding pilot plant. In addition, compositions of salts similar to those of the deposits found on samples tested in the pilot plant were also used in the laboratory experiment. Two commercial steels, P92 and T22, as well as two different aluminides coatings deposited on them were tested both in the laboratory scale rig and the in the pilot plant in order to compare the results.

2. Experimental

2.1. Materials

The substrates were T22 ferritic steel and P92 ferritic-martensitic steel (see Table 1), which are commonly used for high-temperature applications in super-heater tubes and steam pipes [23–25]. Coupons of both steels (20 × 10 × 3 mm) were cut from tubular sections obtained from Vallourec. The specimens were ground with SiC grit paper up to P180, degreased in an ultrasonic bath using isopropanol and deionized water, and subsequently dried with dry air before testing or coating. An environmentally friendly Cr^{+6} free, water based Al slurry developed by INTA was deposited on T22 and P92 surfaces by means of an airbrush. The amount of sprayed slurry is manually regulated by means of a needle controlled by a screw. The applicator simply verifies that the sprayed cloud is homogeneous. An air inlet pressure of 2 atm. is used and the distance from the airbrush to the specimen is kept at approximately 15 cm. Two diffusion heat treatments were then carried out under nitrogen flow to produce different microstructures for the aluminide diffusion coatings: 1) at 700 °C for 10 h and 2) at 1050 °C for 35 min and 795 °C for 70 min. After these treatments, the specimens were rubbed with a Scotch Britte sponge to remove undiffused slurry residues (bisque).

The fuel selected for the study was a mixture of sub-bituminous coal from Puertollano, Spain, and *Cynara Cardunculus* also known as thistle, which is an energy crop grown in the Mediterranean area. The proximate (moisture content, ash content and volatile matter) and ultimate

Table 2
Fuel analysis.

	Coal	Thistle		Coal	Thistle
Proximate analysis (wt. %)			*Calorific value, d.b. (MJ/kg)*		
Volatile matter	24.5	70.9	**HHV, MJ/kg**	18.7	15.2
Ash	38.7	10.0	*Ash analysis (%, d.b.)*		
Moisture	3.6	7.1	**Al_2O_3**	9.2	0.9
Ultimate analysis (% by mass, d.b.)			**CaO**	0.4	2.9
C	44.0	42.3	**Fe_2O_3**	1.9	0.2
H	3.5	6.2	**K_2O**	0.8	2.2
N	1.2	0.7	**Na_2O**	0.1	0.6
S	0.8	0.2	**MgO**	0.4	0.5
O	11.6	39.8	**P_2O_5**	0.05	0.3
Cl	0.08	0.7	**SiO_2**	22.2	0
			TiO_2	0.3	0

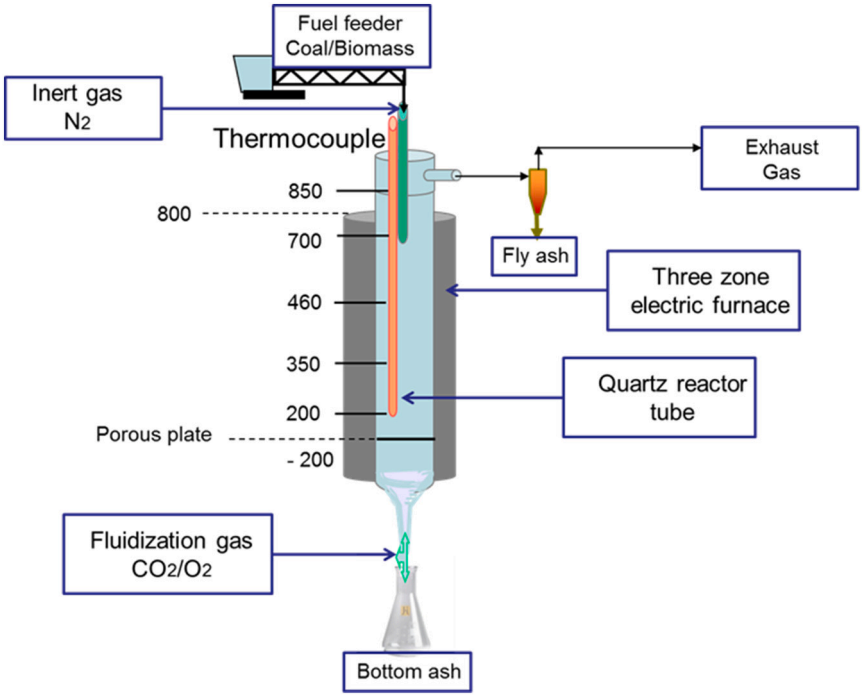

Fig. 1. Scheme of the fluidized bed reactor.

(elemental chemical composition) analyses of the fuel (see Table 2) were conducted by means of a LECO Truspec equipment. Independent IR detectors were used for the simultaneous detection of carbon, hydrogen and sulfur. Nitrogen was measured using a thermal conductivity detection system. Inductively coupled argon plasma atomic emission spectrometry (ICP-AES), by means of a simultaneous spectrometer (Thermo Jarrell Ash model IRIS AP) was used to quantify the minor elements content in fuels (ash analyses). The sub-bituminous coal exhibits a medium range sulfur content while the employed biomass (thistle) has a very high chlorine content. Both fuels were air dried and crushed to 100 μm size particles using a Retsh ZM100 mill.

2.2. Pilot plant co-firing tests

Experiments were performed in a laboratory-scale 0.5 kWh bubbling fluidized bed (BFB) combustor, developed and operated by CIEMAT (Fig. 1). The lab-combustor consists of a vertical quartz reactor tube (length: 1250 mm length; internal diameter: 50 mm) heated by a built-in three zone electric furnace, and three s K-type thermocouples. Inside the reactor, fuel solid particles fed from the top are suspended by an upward

Fig. 2. Image of the test specimens inside the reactor.

controlled flow of a hot gas mixture simulating oxy-fuel combustion conditions. The lower zone of the furnace, below the porous plate, is used to pre-heat the reactant gas, which is introduced in the reactor through the lower section of the reactor tube, while the upper zone is kept as isothermal as possible. A series of thermocouples allow obtaining the axial temperature profile. Each gas is fed independently using a mass flow controller through a mixing zone placed at the base of the quartz tube. The out-coming gases are released through a side-arm at the top end of the tube, being conducted to a particulate control system, prior to gas analysis. The system provides continuous fuel feeding by means of an inert carrier gas (N_2).

In this reactor, a BFB combustion process is simulated, with the fuels being combusted in suspension by a controlled upward flow. The main difference with a real BFB combustor is the absence of bed solids (sand or sorbent). To prepare the fuel, 40/60 (wt%) of thistle and coal respectively were mixed, ground together with a Retsch brand mill, ZM 20, and sieved to obtain the desired granulometry 100–200 μm). This relatively small particle size range has been employed in order to limit the temperature rise within individual particles. The fuel is dosed at a rate of 1 g/min by a gas-tight feeding system on top of the reactor consisting of a particle silo, a screw conveyor and a vibrating feeder. An injection probe has the purpose to guide the particles to the reactor tube inlet and in parallel, the use of the inert gas minimizes reactions. Particles are heated by radiation and convection giving rise to the corresponding combustion reaction compounds. The gas introduced from the bottom is a mixture of 70 vol% CO_2 and 30 vol% O_2 to simulate oxy-fuel combustion conditions. The total flow gas was 3600 l/min. The flow passes a honeycomb structured flow straightener before entering the reaction pipe in order to distribute the gases without any preferential paths.

A multipoint thermocouple is inserted inside the reactor with five temperature sensors longitudinally distributed at 200, 350, 460, 700 and 850 mm (T1-T5, respectively) from the porous plate located at the bottom. A temperature controller is available for each of the three heaters, and can therefore be controlled independently. The measured temperature range for this experiment was 600–620 °C. Three specimen per each coated and uncoated material were placed in the center of the reactor with their surfaces perpendicular to the gas flow as shown in Fig. 2 and were located between sensors T2 and T3.

All specimens were measured to determine the total surface area exposed to the corrosive environment, cleaned in ethanol and weighted in a AND ER-120A balance with ±0.0001 g accuracy. After each test, fly ashes were collected from both the tube walls at the container placed at the bottom of the reactor (Fig. 1). The composition of the combustion gas was monitored during the test by Fourier transformed infrared, FTIR (Gasmet DX 5000), excepting O_2 which was determined by a paramagnetic oxygen analyzer (Fuji Electric). As the fuel feeder of the pilot plant could not operate unattended, the exposure was interrupted every day, running for 8 h per day in stationary mode (weekends excepted). This operation was repeated continuously up to a total of 500 h of exposure.

2.3. Laboratory tests

For the laboratory experiments, prior to testing the uncoated specimens were also measured to determine the total surface area exposed to the corrosive environment, ground with SiC P180 paper, cleaned in ethanol and weighted in a AND ER-120A balance with ±0.0001 g accuracy. The coated specimens were also measured and weighted after removing the bisque. All samples were then coated with a mixture of 45 wt% KCl (AppliChem PANREAC) and 55 wt% K_2SO_4 (AppliChem PANREAC) dissolved in deionized water and heated with a blow dryer to

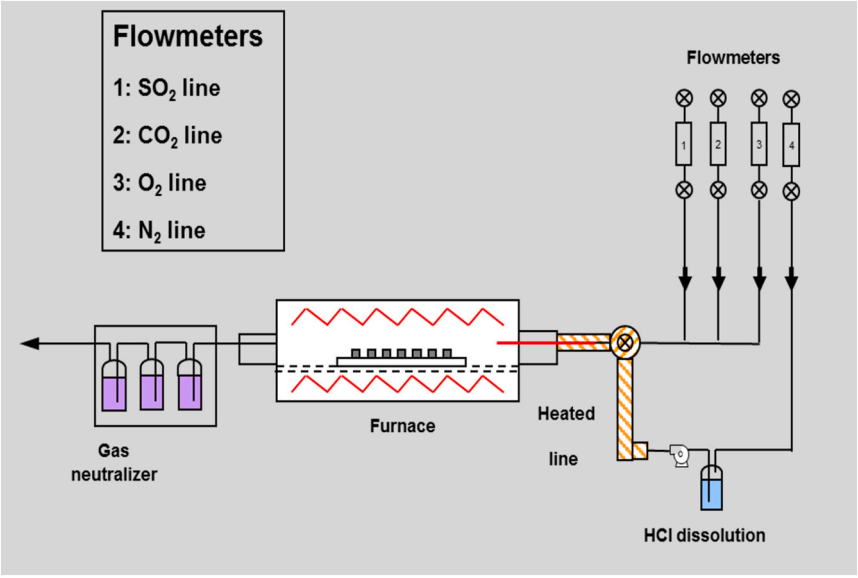

Fig. 3. Laboratory corrosion test rig simulating coal/biomass combustion under low oxy-fuel conditions.

Table 3
Atmosphere test laboratory composition.

O_2	CO_2	H_2O	N_2	SO_2	HCl
vol%	vol%	vol%	vol%	vppm	vppm
8	60	30	2	2	500

evaporate the water. This process was repeated if necessary to adjust the deposit to 0.4–0.7 mg/cm^2 after drying. The tests were performed using an experimental especially designed rig shown in Fig. 3, with four independent gas lines feeding a tubular quartz reactor placed in a furnace. To introduce water vapour and HCl, a deionized water dissolution with the proper concentration of HCl was fed to the reactor by means of an HPLC pump (Eldex Optos Series 5963 1LM 3/32″) through a heated line.

The samples were placed in alumina crucibles, with the large surfaces parallel to the flowing gases with the composition indicated on Table 3, at atmospheric pressure. The exhaust gas was neutralized by bubbling it through alkaline solutions. The test begins by flowing nitrogen for 1 h while the furnace is heating up to the test temperature. Once it is reached, the nitrogen flow is closed and the corrosive gases introduced at a linear velocity of 0.22 cm/s. The test was stopped at 24, 120, 240, 384 and 500 h to weight the specimens by cutting the corrosive gas mixture, flowing nitrogen and turning the furnace off. Cooling to room temperature takes 2 h. To weight each sample, it is cleaned with warm distilled water by dipping the sample while water is being stirred by a magnetic bar for a few seconds, then the sample is sprayed with acetone to accelerate the drying process, dried by means of a blow dryer, weighted and recoated with the salt deposits and weighed again before re-introducing it in the test chamber.

2.4. Characterization techniques

Cross section observations were obtained by cutting the specimens with a diamond wheel ATM 92002401, mounting them in conductive resin Konductomet (Buehler) and polishing with colloidal silica MarterPolish2 (Buehler). The high temperature heat treatment samples were subjected to etching by Vilella's reagent. The cross sections of the as-deposited and oxidized coatings were observed by field emission gun scanning electron microscopy (FESEM) employing a ThermoScientific APREO C-LV microscope equipped with an energy-dispersive X-ray microanalysis system (EDX) from Aztec Oxford.

Crystalline phases were determined by X-ray diffraction (XRD) in a PANalytical X'Pert PRO MRD diffractometer with the help of the Powder Diffraction and Standards (JCPDS) databases. Bragg–Brentano (θ-2θ) at 45 kV and 40 mA ($K_{\alpha 1Cu}$), in the scan range 10°-100° (2θ).

3. Results and discussion

3.1. Characterization of as-deposited coatings

The deposition process of the slurry aluminide coatings have been detailed elsewhere [26]. The two aluminide coatings have been previously characterized by FESEM-EDX and XRD. Fig. 4 shows the cross-section micrographs - taken with the backscattered electron (BSE) detector- of the LTAl and HTAl coatings deposited on T22 and P92 steels, with the corresponding crystalline phases (confirmed by XRD). The main composition and morphological features of each of them are summarized in the paragraphs below, to properly understand the coating morphological and compositional changes after the corrosion tests.

3.1.1. Low temperature aluminide coating (LTAl)

The LTAl coating has demonstrated excellent behavior under simulated corrosive environments at lab scale such as supercritical steam [27], molten nitrates and carbonates [28], and coal oxy-combustion conditions [17,29]. Its microstructure and phase composition resulting from a heat treatment at 700 °C for 10 h has been widely studied in previous works [16].

As shown in Fig. 4, the diffusion LTAl coating, on both steels, is composed by two main layers. The outer thick zone constituted by Fe_2Al_5 with 55 wt% of Al at the surface, whereas the thinner, inner layer is FeAl. The thickness of both coatings (~60 μm) is rather homogenous. The aluminide deposited on P92 exhibits Al_9Cr_4 rich precipitates in higher proportion than on T22 steel, due to the higher Cr content of P92. Indeed, the Cr content near the surface measured by EDX, was 0.8 and 4 wt% for coated T22 and P92 steels, respectively. Some thickness-

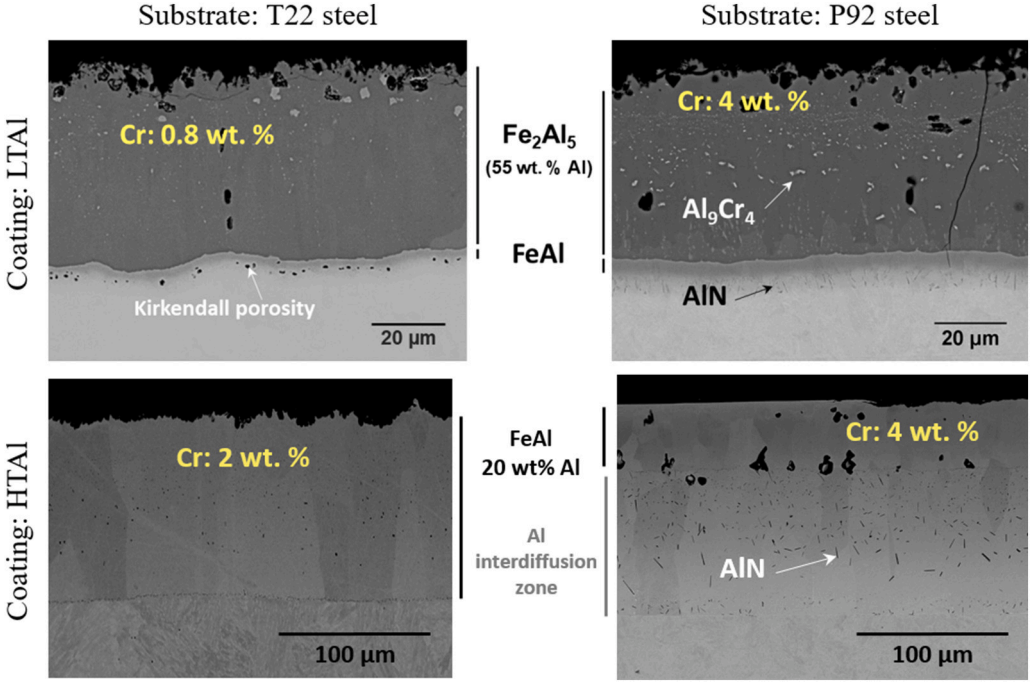

Fig. 4. FESEM micrographs – in BSE- of the cross-sections of T22 and P92 steels coated with LTAl and HTAl coatings.

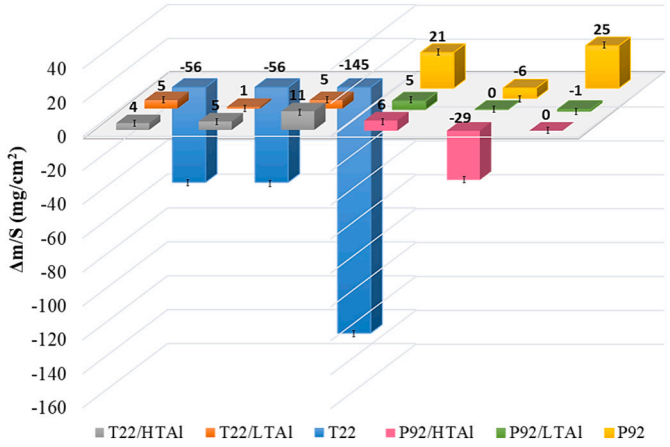

Fig. 5. Mass variation per unit area of uncoated and coated T22 and P92 steels; tested at lab (600 and 650 °C) and pilot (600–620 °C) scales for 500 h.

through cracks appear, but do not cause delamination of the coating, and likely develop during cooling after the heat treatment, as a result of the different phases thermal expansion coefficients mismatch. In addition, coated T22 shows Kirkendall porosity at the substrate-coating interface in contrast to P92. This may be related to the difference in composition of the two alloys which surely affects the diffusion coefficient of the different species. Below the coating, P92 exhibits AlN precipitates, which are absent in T22. Indeed, P92 has higher N content than T22 (Table 1).

3.1.2. *High temperature aluminide coating (HTAl)*

As for the LTAl coating, the HTAl has also been exposed to steam, coal oxy-combustion gases [17], as well as molten carbonates [30]. Its heat treatment is similar to the austenitizing-tempering treatment which is part of the P92 steel manufacturing process (1050 °C for 35 min and 795 °C for 70 min). This coating's microstructure and thickness (120 μm) is quite different from those observe in the LTAl coating (see Fig. 4). Instead of Fe_2Al_5, which is present in LTAl, a top layer of FeAl with 20 wt % of Al at the surface is present in the HTAl coating on both steels, as a result of faster and deeper reaching Al-Fe interdiffusion. In the case of coated P92, the internal Al interdiffusion zone exhibits acicular AlN precipitates in larger quantities and dimensions than those detected in the LTAl coating on the same substrate. On T22, AlN precipitates were not observed. As mentioned, the N content on T22 is significantly lower than in P92. Another difference is that on P92 the coating exhibits large pores that mostly accumulate at the interface with the interdiffusion zone, whereas on T22 no porosity was observed. No through-thickness cracks could be found in these two coatings. The Cr surface content of the HTAl coating deposited on the T22 steel was lower (2 wt%) than in the P92 steel (4 wt%).

3.2. *Characterization of tested uncoated and coated substrates exposed to biomass corrosion*

The mass variation of all uncoated and coated T22 and P92 steels have been followed through an isothermal, discontinuous corrosion tests performed at 600 and 650 °C under a model oxy-combustion atmosphere in the laboratory and at 600–620 °C in a pilot plant up to 500 h. It must be kept in mind that in the pilot plant temperature is not as stable as in the lab as fuel is being burnt. Fig. 5 shows that variation of mass per unit area (Δm/S) after 500 h of exposure.

In the case of T22 substrate, similar high mass losses were observed in the lab at 600 °C and in the pilot plant (-56 ± 1 mg/cm^2), whereas at 650 °C the mass loss was significantly higher (-145 ± 1 mg/cm^2). This is attributed to a spallation of the oxide layer that forms on the surface (see Fig. 6).

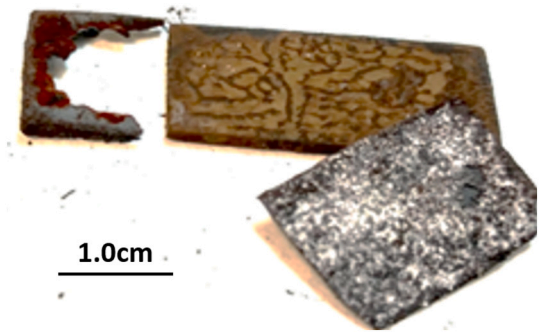

Fig. 6. Image of a sample of uncoated T22 steel tested at lab (650 °C) scale for 500 h.

Based on the information provided in Fig. 5, low magnitude mass gains occur for the LTAl coating on T22 steel samples in the three studied test conditions, with the pilot plant exposed specimen exhibiting the lowest mass gain (1 ± 1 mg/cm^2) whereas the two lab tested specimens gained 5 ± 1 mg/cm^2. On the other hand, the HTAl coated T22 sample exposed to 650 °C in the lab exhibited a mass gain which was approximately twice as much (11 ± 1 mg/cm^2) as those observed for the other two samples (4 ± 1 mg/cm^2 at 600 °C in the lab and 5 ± 1 mg/cm^2 at 600–620 °C in the pilot plant).

P92 tested in the laboratory at 600 and 650 °C experienced mass gains (21 ± 1 and 25 ± 1 mg/cm^2, respectively). However, for the sample tested at 600–620 °C in the pilot plant, there was a relatively low mass loss of 6 ± 1 mg/cm^2. On the other hand, the mass variation for the LTAl coating on P92 tested in the lab at 600 °C is 5 ± 1 mg/cm^2 and -1 ± 1 mg/cm^2 for the sample exposed at 650 °C for 500 h, whereas for the sample tested in the pilot plant there was no significant mass variation. The mass variation for the HTAl on P92 is 6 ± 1 mg/cm^2 for the sample tested at 600 °C and 0 ± 1 mg/cm^2 for the sample tested at 650 °C. Surprisingly, the sample exposed to 600–620 °C in the pilot plant, experienced a mass loss of -29 ± 1 mg/cm^2.

Overall, these gravimetric results (Fig. 5) indicate that in general, the coatings performed considerably better than the uncoated substrates with the exception of the HTAl coating on P92. However, the mass variation cannot be used to establish the corrosion kinetics for the uncoated substrates due to spallation under the present conditions. Moreover, during the process of sample preparation for metallographic studies, spallation of loosely adhered scales also took place. For future studies, full descaling by means of acid etching is recommended in order to determine the corrosion kinetics using the alloys mass loss. In addition, the slurry aluminide coatings exhibit high roughness levels so the actual Δm/S value calculated by simply measuring the sample dimension, provides a value higher than the real one that could be obtained if the real surface of the specimen could be measured. Another issue that adds uncertainty to mass variation measurements in this case, is the fact that when heat treating slurry coatings, a bisque composed of oxidized undiffused slurry particles is always observed. This bisque is removed by gently rubbing with a Scotch Brite sponge but often some residues remain attached to the specimen surface, and during exposure to high temperature oxidation it spalls. Therefore, for the coatings also, mass variations cannot be used to establish corrosion kinetics, and only an idea of the behavior when comparing to the uncoated material can be obtained.

The cross-sections of the T22 and P92 uncoated substrates after being tested for 500 h at the lab (600 and 650 °C) and the pilot (600–620 °C) plant are shown in Fig. 7. Firstly, the BSE micrograph of the T22 steel exposed up to 600 °C shows loosely attached scales which delaminate in agreement with the observed corresponding weight loss. Different morphology zones can be perceived, and according to the element map obtained by EDX: the outermost half is rich in O and Fe whereas the inner zone appears more compact, and also contains Cr and some S. In

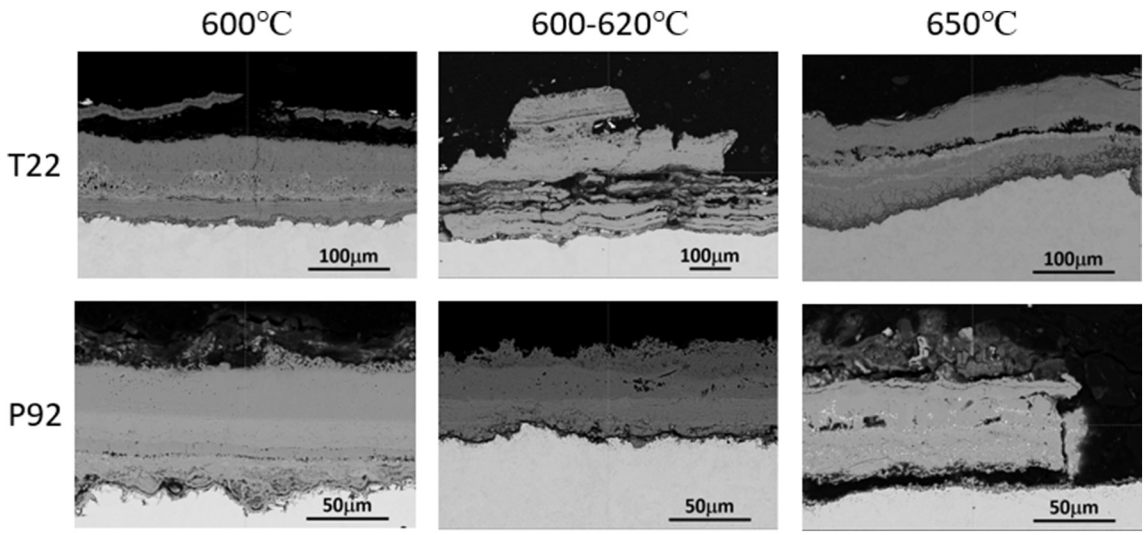

Fig. 7. FESEM micrographs – in BSE- of the cross-sections of uncoated T22 and P92 steels; tested at lab (600 and 650 °C) and pilot (600–620 °C) scales for 500 h.

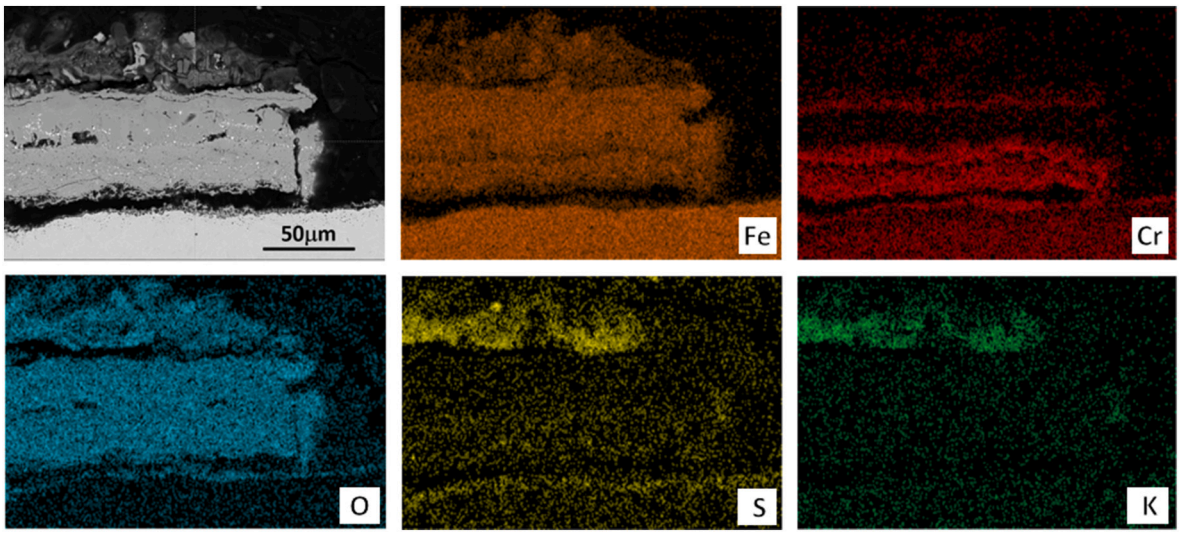

Fig. 8. FESEM micrograph – in BSE- and EDX element mapping of the cross-section of uncoated P92 steel; tested at lab (650 °C) scale for 500 h.

addition, internal corrosion was observed occurring preferentially through the grain boundaries.

The cross-section of the P92 sample also tested at 600 °C (Fig. 7) exhibits a darker zone rich in S, K and O on top of the oxide multi-layers (EDX not shown), which in some cases exhibit porosity. Again, the outermost layer is rich in Fe and O, the next lighter layer is rich in Cr, and it is located over a pore rich inner zone which exhibits low Cr content. Finally, in close contact with substrate there is a layer rich in Cr and S. Corrosion proceeds through grain boundaries as it can be observed on T22 after 500 h at 650 °C as the grain morphology is maintained after oxidation has taken place. P92 exhibits weight gain in general, whereas T22 experiences weight loss or very little gain. This is coherent, as on P92, the observed oxides and other corrosion products remain adhered. On the other hand, on T22 spallation takes place, probably due to the higher thickness, which implies higher stresses at the oxide-substrate interface.

The cross-section of the T22 sample tested at 600–620 °C in the pilot plant (Fig. 7), exhibits a very thick oxidation layer with evidence of delamination and detachment due to poor cohesion and adhesion and also to the high thickness of the layer (>200 μm). Despite the presence of this very thick layer, this sample experienced significant weight loss (Fig. 5), indicating that oxide has reformed after detachment. On the other hand, P92 shows a different appearance with a denser oxide layer with <100 μm. Again, two distinct composition areas were observed according to EDX analysis (not shown): the outer one is rich in Fe and O, while the inner also exhibits is Cr. In this case weight loss is also observed so scale detachment and reformation must have taken place. The interface with the substrate is rich in S.

The cross-sections of the T22 and P92 samples tested at 650 °C also show extensive oxidation and evidence of longitudinal cracking and delamination, in particular for T22, which coincides with the large mass loss observed in Fig. 7 in the case of T22. Moreover, a large degree of intergranular corrosion can be observed in particular, in the oxide scale developed by T22. In the case of the P92 substrate the oxidation is also severe. Fig. 5 shows an increase in mass for this alloy at 650 °C, but there is nevertheless, evidence of delamination and spallation in the observed oxide, but perhaps at a lower extent in comparison with T22. As in the other exposed samples, two distinct composition layers are observed for both substrates. Fig. 8 shows the element mapping of P92 exposed at 650 °C for 500 h in the laboratory where a Cr and S enriched thin layer can be seen right at the interface with the substrate, in analogy with other exposures carried out under SO_2 containing atmospheres [22]. The

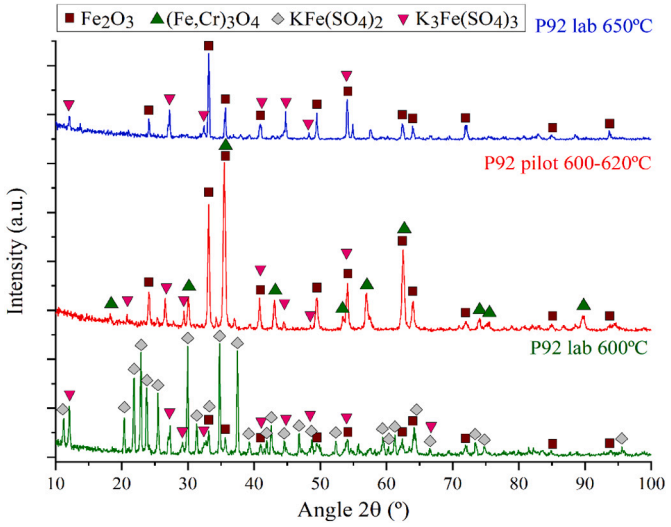

Fig. 9. XRD patterns of uncoated P92steel; tested at 600 and 650 °C lab (600 and 650 °C) and pilot (600–620 °C) scales for 500 h.

presence of chromium sulphide has been confirmed by other authors when P92 is exposed to SO_2 containing atmospheres [31].

In addition, the element maps show that the outermost corrosion products are rich in Fe, S and K and correspond likely to $KFe(SO_4)_3$ and $K_3Fe(SO_4)_3$ which were detected by XRD as shown in Fig. 9. The other main peaks can be assigned to Fe_2O_3. On the other hand, in the P92 specimens tested at 600–620 °C in the pilot plant, $(Fe,Cr)_3O_4$ is also present whereas the peaks corresponding to $KFe(SO_4)_3$ are absent. In the lab at 600 °C only peaks corresponding Fe_2O_3 could be detected.

Fig. 10 shows the FESEM cross-sections of the P92 and T22 substrates coated with LTAl and tested under the three conditions described above. In these six images it can be seen how the samples tested at 600 °C in the laboratory and at 600–620 °C in the pilot plant, reveal a similar coating microstructure for both substrates. Therefore, the degradation of the coatings appears similar both cases. In contrast, an as expected, the samples tested at 650 °C in the laboratory, show microstructural changes, since at 650 °C the interdiffusion of aluminum with the substrate is much higher than at lower temperatures.

Fig. 11 compares FESEM-EDX element mappings performed on the cross-sections of the LTAl coating on P92 after exposure to all corrosion environments. It can be seen how at 600 °C in the laboratory has suffered little degradation compared to the as-deposited coating (Fig. 4), approximately maintaining the initial thickness. The Cr rich layer within the coating corresponds to a zone with a concentration of Cr aluminide precipitates which is present in the initial coating. The specimen exposed in the lab at 600 °C exhibits a thicker darker zone on the coating's surface and, as observed in the element mapping showed also in Fig. 11, this zone is rich in O, S, K and Al, and exhibits two different morphology layers.

Indeed, the corresponding XRD pattern (see Fig. 12) includes high intensity peaks that correspond to $KAl(SO_4)_2$ and $K_3Al(SO_4)_3$ and the original coating phase Fe_2Al_5. Some very low intensity peaks corresponding to FeAl can also be observed. In addition, porosity has developed at the surface, immediately below the corrosion products layer, and above the Cr enriched zone which correspond to Cr aluminides precipitates as already mentioned (Fig. 10). At the surface, Al is depleted by reaction of the coating with the deposits and gases and it should be replenished by more Al coming from the coating's bulk. However, the Cr precipitates enriched area may block this process, and vacancies develop in the area above, as a result of Al outwards diffusion. The presence of FeAl islands within the Fe_2Al_5 matrix can be also observed and is likely due to Al inwards diffusion at 600–620 °C and the resultant reduction in the Al content of the intermetallic phase Fe_2Al_5.

The P92 coated sample tested in the pilot plant exhibits the same microstructure and also a darker zone on the surface, but it is thinner than that observed on the specimens tested in the lab at 600 °C. This zone is rich in Al and O and also contains some Fe, S and K, as shown in the corresponding element mapping (see Fig. 11). However, the XRD pattern of this sample shows no peaks corresponding to the corrosion products $KAl(SO_4)_2$ and $K_3Al(SO_4)_3$ observed in the lab, rather exhibiting low intensity peaks that match phase of Fe_2O_3 (Fig. 12).

The evolution of the LTAl coating on T22 after testing at 600 °C is similar to that described in the previous paragraph for P92. But, since it has a lower chromium content (2 wt% compared to almost 9 wt% for P92), the chromium-rich zone observed for coated P92 does not form and the large pores observed at its surface are also absent. However, some degree of porosity appears at the coating-substrate interface in this case. In analogy with the LT aluminized P92, the lab tested specimen at 600 °C is quite similar to that tested in the pilot plant at 600–620 °C.

The samples tested at 650 °C for 500 h, in the laboratory on both substrates exhibit significant microstructural changes due to a higher level of coating-substrate interdiffusion as a result of the higher temperature (see Fig. 10). Al has diffused inwards and Fe outwards, so that

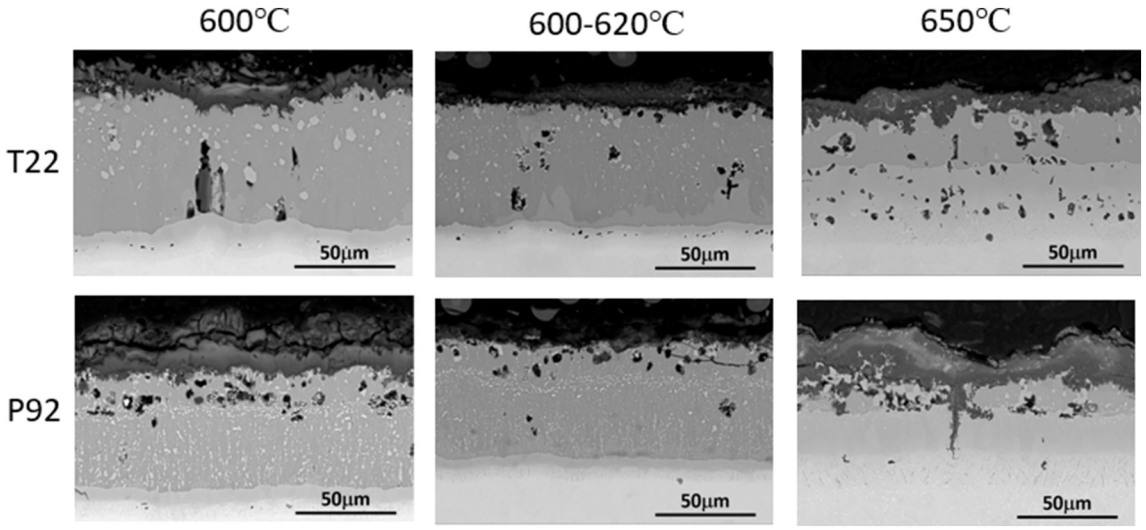

Fig. 10. FESEM micrographs – in BSE- of the cross-sections of T22 and P92 coated steels with LTAl; tested at lab (600 and 650 °C) and pilot (600–620 °C) scales for 500 h.

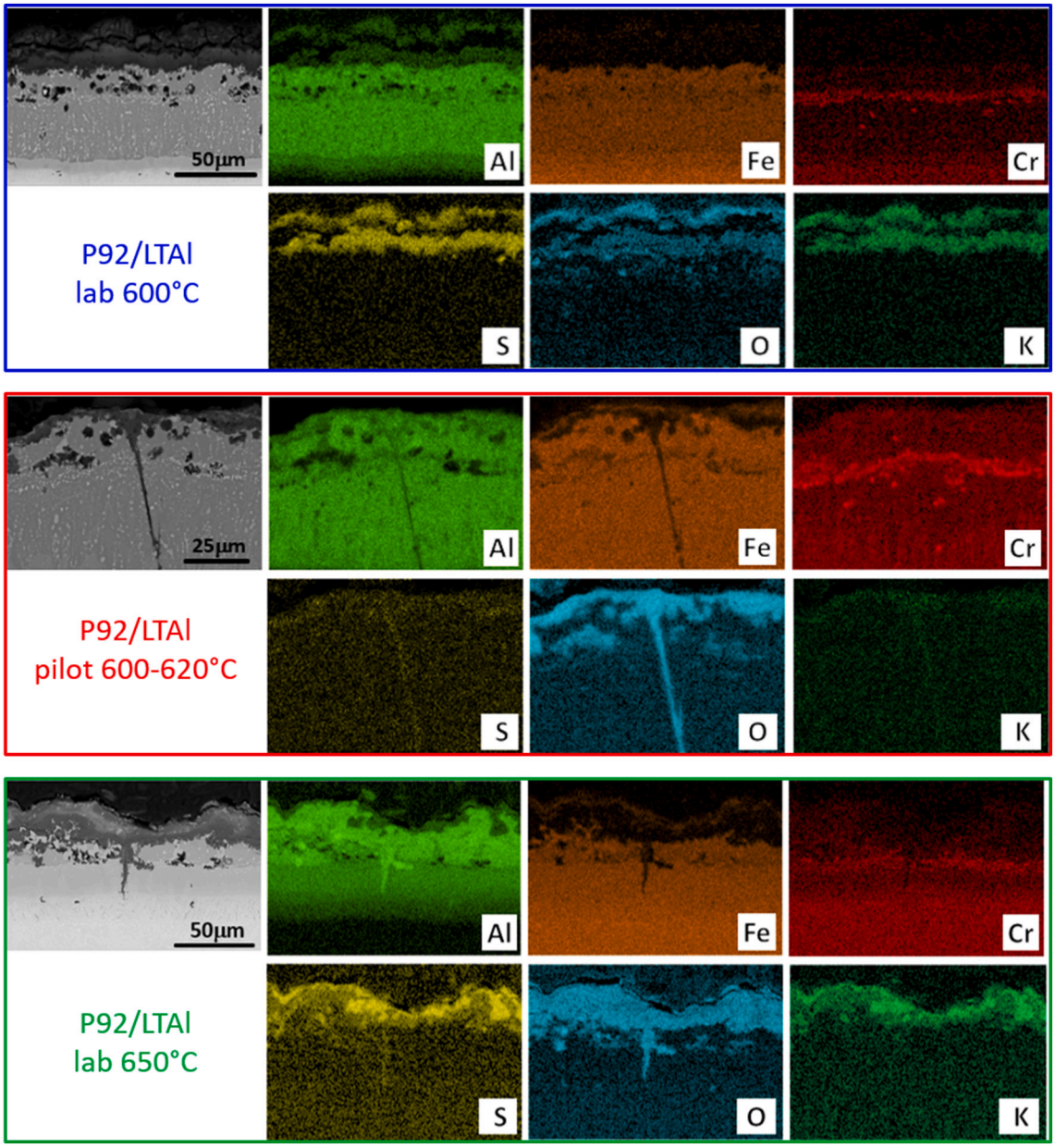

Fig. 11. FESEM micrograph – in BSE- and EDX element mapping of the cross-sections of P92 steel coated with LTAl; tested in the lab (600 and 650 °C) and in the pilot plant (600–620 °C) for 500 h.

the Al poorer phase FeAl has increased in thickness at the expense of Fe_2Al_5. Al has also diffused into the substrate causing the development of more AlN precipitates that reach deeper within the substrate [27]. These specimens also show corrosion products on their surface as the samples tested at lower temperature, but in this case the corresponding XRD patterns show that there is mostly $KAl(SO_4)_2$, as peaks that match $K_3Al(SO_4)_3$ were not detected (Fig. 12). Moreover, the cross section of the LTAl on P92 specimen exhibits only one layer on the surface (corresponding to the corrosion products) (Fig. 11). Cracks present in the as deposited coating fill with corrosion products, rich mainly in Al and O as well as minor amounts of S, as observed in the corresponding element mapping shown on Fig. 11 too. Said cracks do not propagate and also do not become pathways for the corrosive media to reach the substrate.

Fig. 13 shows the FESEM cross sections of the P92 and T22 substrates coated with the aluminide coating heat-treated at higher temperature (HTAl) and tested under the three conditions described above. In the images it can be seen how the samples tested at 600 °C in the laboratory and at 600–620 °C in the pilot plant, show different corrosion microstructures and different degradation rates for both substrates. The deterioration produced on the coated T22 samples is higher than on the P92 samples. On the T22 substrate, there is significant loss of the coating for the sample tested at 600–620 °C whereas total loss for the sample tested at 650 °C and also spallation. At 600 °C in the lab, the HTAl coating deposited on T22 showed an important development of Kirkendall porosity at the interface between the FeAl layer and the coating-substrate interdiffusion zone which appears to be coalescing.

EDX element mapping of the HTAl coating deposited on T22 and tested at 600 °C in the lab is compared in Fig. 14 with the same material system exposed in the pilot plant (600–620 °C). The lab tested sample showed the presence of Al oxide and some S within the pores. Al oxide was also present and on the top surface of the coating, with other corrosion products rich in S and K as well, which corresponds to $KAl(SO_4)_2$ and $K_3Al(SO_4)_3$ as confirmed by the XRD pattern (not shown). On the other hand, the sample tested at 600–620 °C developed a thick layer

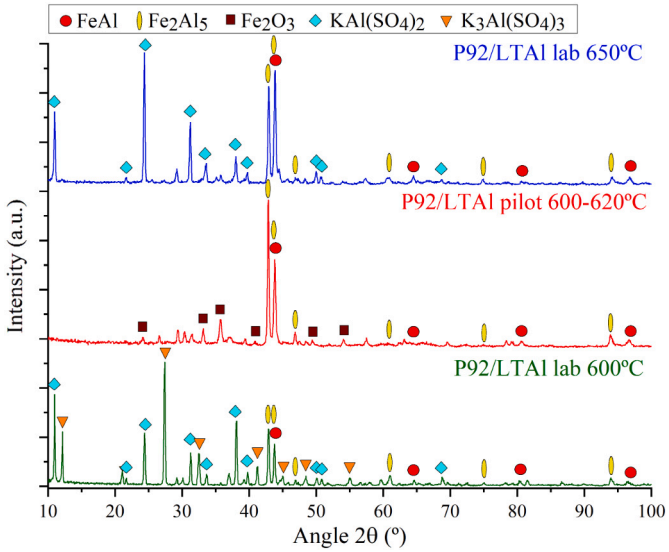

Fig. 12. XRD patterns of P92 steel coated with LTAl; tested in the lab (600 and 650 °C) and in the pilot plant (600–620 °C) for 500 h.

of corrosion products, whereas the coating was been lost to only about 1/4 of the pristine coating thickness. Therefore, the coating-substrate interdiffusion zone was exposed, and developed a layered oxide rich in Al, Fe and some Cr as observed in the EDX element mapping without S and K. At 650 °C the degradation of the coating has been total, with no remains of the initial coating.

In the case of P92 coated with HTAL (see Fig. 13), it can be seen how there is no significant porosity development within the coating at 600 °C and a layer of corrosion products can be seen on the top of the coating but without significant degradation compared to the initial coating (Fig. 4). Degradation of the coating tested at 600–620 °C is higher, with evident FeAl coating thickness reduction and local corrosion penetration within the coating substrate interdiffusion zone, can be observed in isolated areas as shown in Fig. 15, but without reaching the substrate. Very likely, penetration has occurred through cracks that may have been developed to a higher extent in the pilot tested samples due to the higher number of cycles to which they were exposed. The remaining coating is covered by mixed Al, Fe and Cr rich oxides. Also in Fig. 15, the EDX mapping illustrate how the wide crack self-heals, filling itself with Al rich oxide. In addition, it can be observed how corrosion propagates through grain boundaries within the coating as well as laterally at the coating-interdiffusion zone interface. Finally, the coating tested at 650 °C equally showed significant degradation of the FeAl layer to about 1/3 of the original thickness left, but still showing some degree of protectiveness. Degradation has occurred but to a substantially lesser extent than in the T22 specimen.

In addition, Fig. 15 exhibits the EDX the element mapping of this coating at 650 °C showing the complex corrosion products, containing O, S and K, Al, Fe and some Cr over an Al rich thin oxide over the coating. The main difference between the coating composition on P92 and T22 is the Cr content, higher in P92, so the results may indicate that Cr plays a critical role in maintaining a protective scale on the coating's surface.

The XRD patterns corresponding to the coated P92 specimens include high intensity peaks that were assigned to $KAl(SO_4)_2$ and $K_3Al(SO_4)_3$ as well as to the original coating phase (FeAl) (Fig. 16) for the coatings tested in the laboratory at 600 °C and 650 °C. For the sample tested in the CIEMAT pilot plant at 600–620 °C, the phases corresponding to the corrosion products $KAl(SO_4)_2$ and $K_3Al(SO_4)_3$ do not appear, confirming the EDX analyses results. Rather, high intensity peaks assigned to Fe_2O_3 can be observed. The XRD of the coated T22 tested specimens showed the same products.

4. Discussion

The results obtained in this comparative study indicate that the model laboratory atmosphere produces similar results to those obtained in a pilot scale plant, taking into account the temperature variations associated with pilot plant operation.

The behavior observed for the uncoated substrates indicate significant spallation for all test conditions, so no kinetic data could be obtained. Low alloyed ferritic steels experience severe corrosion in Cl containing environments as iron chloride forms and evaporates due to its high vapour pressure at temperatures higher than 550 °C ($2.1{\cdot}10^{-4}$ atm at 550 °C). The developed oxides are loose and do not provide sufficient protection. In addition, if molten salts are present (in particular chlorides), protective Cr rich oxides will dissolve forming chromates, which are not protective [32]. On the bases of the large weight loss, the corrosion rate was much higher for T22 than for P92, confirming that a higher Cr content (in P92) ensures a relatively higher degree of protection as observed by others [33].

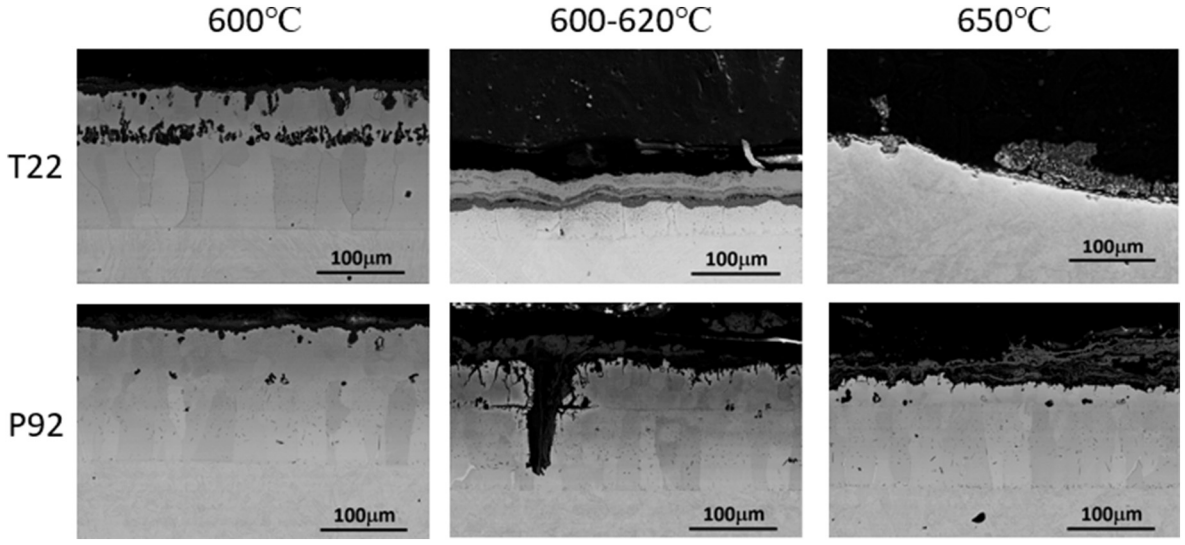

Fig. 13. FESEM micrographs – in BSE- of the cross-sections of T22 and P92 steels coated with HTAl; tested in the lab (600 and 650 °C) and in the pilot plant (600–620 °C) for 500 h.

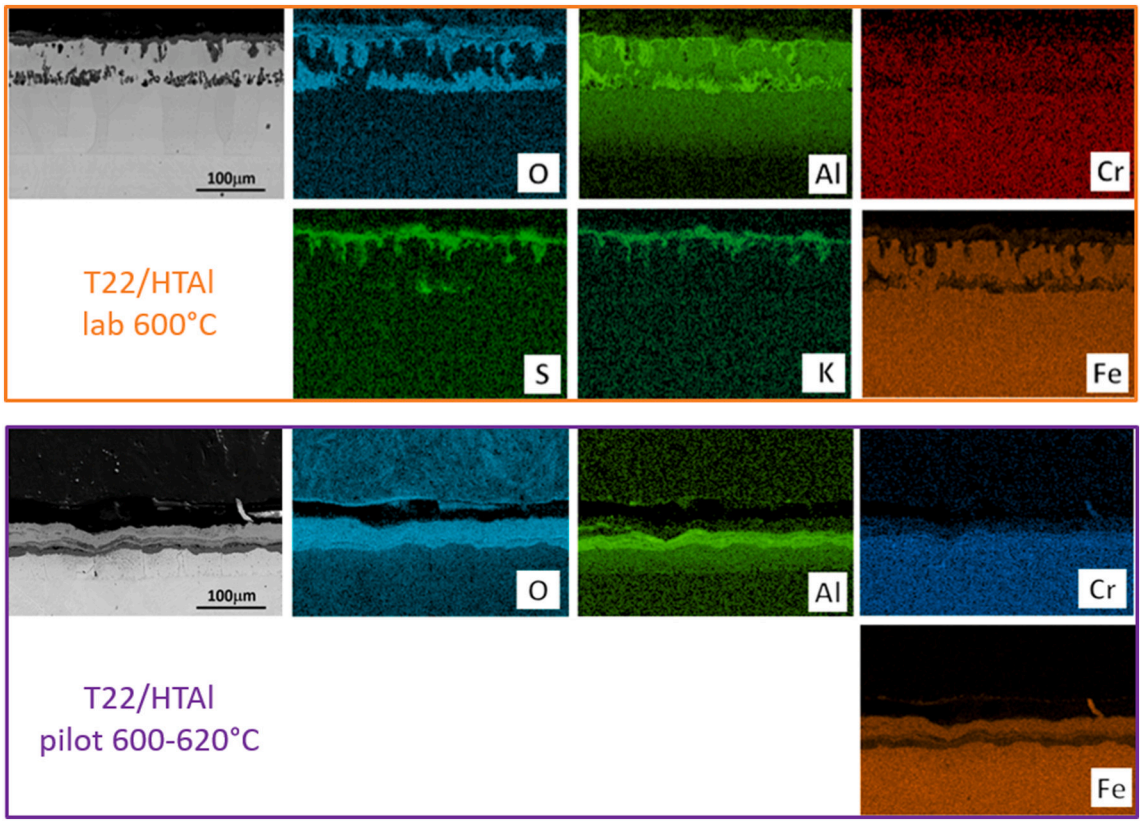

Fig. 14. FESEM micrograph – in BSE- and EDX element mapping of the cross-sections of T22 steel coated with HTAl; tested in the lab (600 °C) and in the pilot plant (600–620 °C) for 500 h.

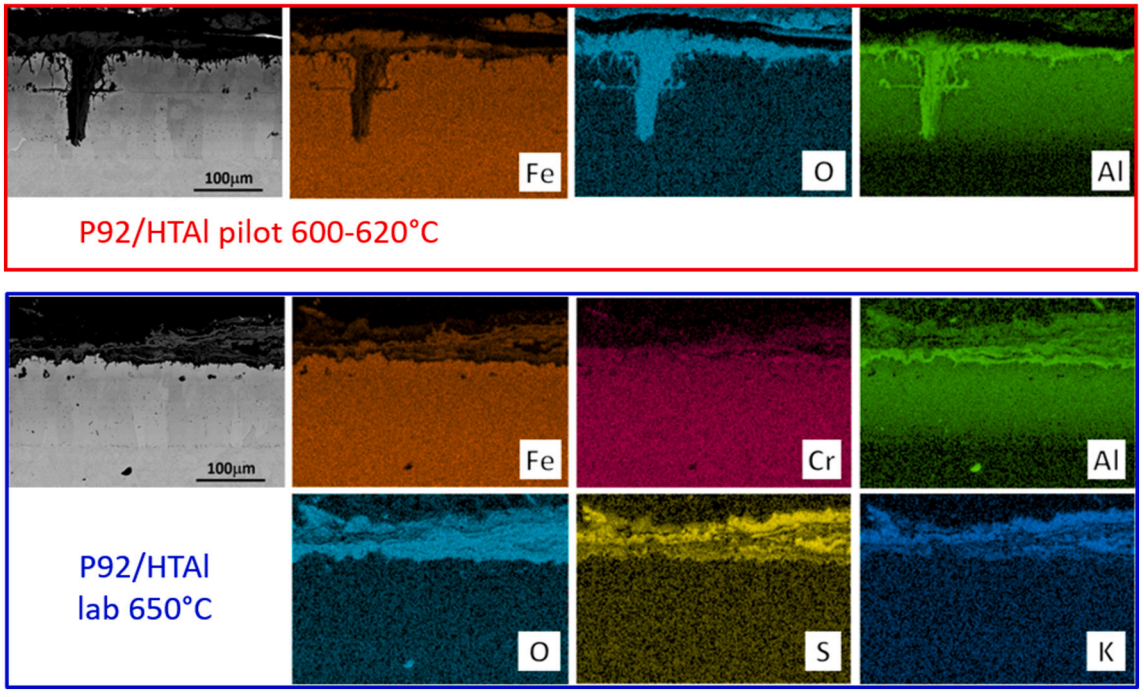

Fig. 15. FESEM micrograph – in BSE- and EDX element mapping of the cross-sections of P92 steel coated with HTAl; tested at the pilot plant (600–620 °C) and at the lab (600 °C) for 500 h.

XRD (Fig. 9), in combination with EDX element mappings, showed similar corrosion products for the pilot plant and the 600 °C tested P92 samples which develop Fe_2O_3 and $K_3Fe(SO_4)_3$ scales as corrosion products. (Fe, Cr)$_3O_4$ was also observed in the pilot scale tested specimen; on ferritic steels, Fe_2O_3, and under some conditions Fe_3O_4 form by outward Fe diffusion, whereas under these scales, (Fe, Cr)$_3O_4$ spinels

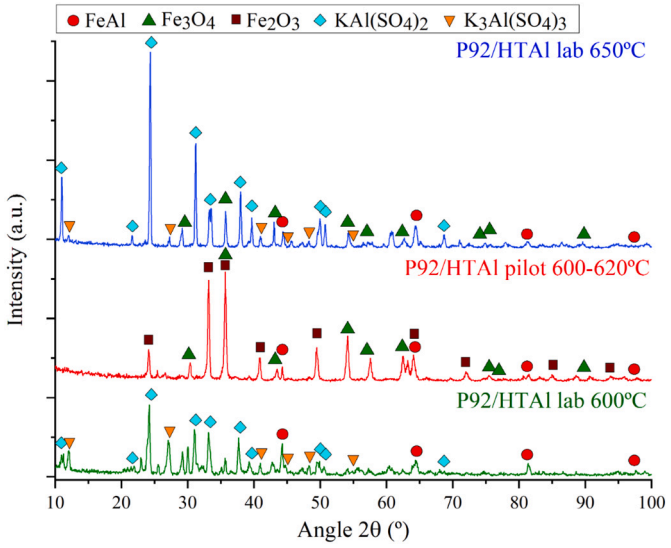

Fig. 16. XRD patterns of P92 steel coated with HTAl; tested in the lab (600 and 650 °C) and in the pilot plant (600–620 °C) for 500 h.

develop by O inward diffusion [34]. Given the abundant observed spallation for all specimens, it is possible that peaks corresponding to $(Fe, Cr)_3O_4$ were picked up in this particular sample (on which no Fe_2O_3 was observed). For instance, in the P92 sampled tested in the lab at 650 °C, the bottom half of the oxide scale is rich in Cr and could very likely correspond to $(Fe, Cr)_3O_4$ spinel (Fig. 8) but could not be picked up by XRD due to being located too deep within the scale.

Other authors [35] have observed $K_3Fe(SO_4)_3$, when using K_2SO_4 deposits in the presence of SO_2, which can be catalyzed by Fe_2O_3 to be transformed in SO_3 [36]:

$$3K_2SO_{4(s)} + 3SO_{3(g)} + Fe_2O_{3(s)} \rightarrow 2(K)_3Fe(SO_4)_{3(s,l)} + 6O_{2(g)}$$

Molten alkali-metal-trisulphates are known to cause accelerated corrosion in super-heater tubes in coal-fired conventional boilers and in biomass-fired furnace, deposits rich in alkali sulphates are also widely reported [32]. The melting point of $K_3Fe(SO_4)_3$ is 615 °C but it can form lower melting temperature eutectics when mixed with $Fe_2(SO_4)_2$ so it could be present in molten state even in the 600 °C exposure as well as in the pilot plant, solidifying upon cooling to room temperature.

Regarding the sample tested at 650 °C, in addition to Fe_2O_3 and $K_3Fe(SO_4)_3$, it also developed $KFe(SO_4)_2$ and judging by the corresponding peaks intensities, it appears to be the main corrosion product. $KFe(SO_4)_2$ melts at 694 °C but it is also less stable than $K_3Fe(SO_4)_3$ and starts to decompose at 650 °C [37].

$$KFe_3(SO_4)_2(OH)_6 \rightarrow KFe(SO_4)_2 + Fe_2O_3 + 3H_2O$$

In contrast to the uncoated substrates, LTAl coated specimens demonstrated a significant degree of protection with little degradation and no evidence of substrate attack, neither on P92 nor on T22. The samples tested at lower temperatures in the laboratory and in the pilot plant showed very similar microstructures. The main change observed relative to the unexposed coating was the presence of a relative thin layer on top of the laboratory exposed specimen. The diffraction pattern of this sample (tested at 600 °C), along with the EDX element mapping, indicate that this layer likely corresponds to $KAl(SO_4)_2$ and $K_3Al(SO_4)_3$. These two species may form from the following reactions:

$$Al_2O_3 + 3K_2SO_4 + 3SO_3 \rightarrow 2K_3Al(SO_4)_3$$

$$Al_2O_3 + K_2SO_4 + 3SO_3 \rightarrow 2KAl(SO_4)_2$$

Al_2O_3 could initially develop on top of the coating in the presence of sufficient water vapour or oxygen. $KAl(SO_4)_2$ can also form from $K_3Al(SO_4)_3$ by thermal decomposition, as it has been observed by Zeng and coworkers [37]. Indeed, on the sample tested at 650 °C in the laboratory, only $KAl(SO_4)_2$ was observed. $K_3Al(SO_4)_3$ exhibits a higher melting point (654 °C) than the corresponding Fe containing salt and therefore may behave as a better corrosion barrier.

Regarding the pilot plant tested specimens, no sulfates could be detected on their surfaces which could be due to the frequent thermal cycling experienced by these samples, which could cause detachment, and also to the fact that no deposits are placed on them prior to testing so a lower accumulation of corrosion product can take place.

Similar results were obtained by Vokál and coworkers [38] when testing a Fe aluminide (Fe_2Al_5) coating deposited on P91 at 650 °C for 300 h under 50:50 mol/mol K_2SO_4/KCl deposits. The aluminide, deposited by pack cementation performed very well although some degradation by interdiffusion was observed.

In contrast, the HTAl coatings behavior was not as good, and complete degradation was observed for coated T22 tested at 650 °C in the laboratory (Fig. 13). These coatings have a lower content of Al at the surface (20 wt% as opposed to 55 wt% for the LTAl coatings). The degree of corrosion was in this case higher in the pilot plant than in the lab at 600 °C and can be explained by the higher average temperature in the plant (600–620 °C). It appears as the Al content of this coating is sufficient only for operation at 600 °C or lower, at least under the present conditions. The Cr content seems to play a role as aluminide coated P92 with a higher Cr content, showed slower degradation than coated T22. Cr is known to reduce the critical amount of Al requires to form a protective scale.

Grégoire and collaborators [39] studied the behavior of slurry aluminide coating, characterized by the FeAl phase (as they were heat treated at 1050 °C) in contact with molten NaCl-KCl at 700 °C. In particular, when using ferritic steel P91 as substrate, the coatings offered very good protection but they were tested for only 100 h. Their results even indicated that iron-rich aluminides offer better protection than nickel-rich aluminides in molten NaCl–KCl.

Kiamehr et al. [40] studied Fe aluminide coatings deposited by pack cementation on P91 under pure thick KCl deposits at 600 °C for 168 h, and observed different results. For coatings richer in Al, including the Fe_2Al_5 phase, degradation occurred across the entire surface and in general, selective removal of Al and formation of voluminous and porous Al-rich corrosion products on top of the coating was observed. Only under few locations the coating had totally disappeared. Surprisingly, for coatings with lower Al content ($Fe_{1-x}Al$) only local attack could be found, and at few locations, both the coating and the underlying alloy were corroded. Their results showed that in local attack zones, significant Al dilution was found while an Al-rich corrosion product has formed. The authors proposed, that the thin Al_2O_3 formed on the coating could be damaged due to the presence of KCl forming KAl_9O_{14} (not observed) or alternatively, an electrochemical mechanism which involves formation of KOH (among other species) which can spontaneously react with Al_2O_3.

Our test conditions in the laboratory were different as K_2SO_4 deposits were also present and the exposures were longer. Several authors have shown that the presence of SO_3 in the gas and sulphates have a beneficial effect as alkali chloride corrosion is reduced because the chlorides are transformed into sulphates which are less corrosive [41,42]. This could explain the difference in the behavior of our coatings relative to the other published data. However, sulphates were not added to the pilot plan test, and the results were quite similar to those obtained in the laboratory in the present study, and under the described conditions. Finally, and by way of summary, Table 4 shows the differences and similarities found in the systems that have shown the best performance against corrosive media both at the laboratory and at pilot plant.

Table 4
Main results from uncoated and coated P92 steel; tested at 600 and 650 °C lab (600 and 650 °C) and pilot (600–620 °C) scales for 500 h.

	Lab 600 °C	Pilot 600–620 °C	Lab 650 °C
P92	Significant spallation: oxides which are no protective and lack sufficient adhesion and cohesion **Fe_2O_3** reacts and forms **$K_3Fe(SO_4)_3$**. This sulfate can accelerate corrosion kinetics, forming eutectics with $Fe_2(SO_4)_2$ and lowering its $T_{f\ K3Fe(SO4)3} = 615$ °C		
	–	**$(Fe,Cr)_3O_4$ is also observed**	+ **$KFe(SO_4)_2$** (main corrosion product), $T_{f,\ KFe(SO4)2} = 654$ °C is higher than $T_{f,\ K3Fe(SO4)3}$ It seems to be less stable.
P92/LTAl	Protective diffusional coating with slight degradation (porosity in the outer zone of the coating). **Fe_2Al_5** (55 wt% Al initial) transforms to FeAl.		
	+ **$KAl(SO_4)_2$**	Very thin layer of surface deposits.	+ **$KAl(SO_4)_2$**
	+ **$K_3Al(SO_4)_3$**.	No presence of sulphates.	
	$T_{f,\ K3Al(SO4)3} = 654$ °C	+ **Fe_2O_3**.	
	Similar microstructure		
P92/HTAl	Relatively protective coating at $T \leq 600$ °C		
	FeAl (20 wt% Al initial)		
	+ **$KAl(SO_4)_2$**	+ **Fe_2O_3**	+ **$KAl(SO_4)_2$**
	+ **$K_3Al(SO_4)_3$**	+ **$(Fe, Cr)_3O_4$**	+ **$K_3Al(SO_4)_3$**
			+ **$(Fe, Cr)_3O_4$**

5. Conclusions

Biomass combustion plants efficiencies can be improved if more corrosion resistant material systems are used. Corrosion testing is therefore critical, and given the variety of corrosive species resulting from biomass, choosing meaningful laboratory test conditions can be very difficult. In this study, information such as gas and deposits composition from a pilot plant test burning coal/biomass, has provided sound indications to design less costly and more controllable laboratory tests. Such investigations has provided meaningful results regarding screening of more corrosion resistant candidate materials to be used in biomass power plants.

Laboratory testing carried out under oxy-fuel combustion conditions, resulted in similar degradation patterns and corrosion products as those obtained on samples exposed in the pilot plant. Certain differences were observed but could be explained to the temperature variations and cycles as the pilot plant test had to be stopped daily. This method of testing can therefore result in more realistic studies as well as ranking of materials and coatings in the laboratory.

Two aluminide coatings with different microstructures and Al contents exhibited a protective behavior under all conditions relative to the uncoated P92 and T22 steels which experience abundant oxide growth and spallation. The coating with the higher Al content survived all the tested conditions whereas the lower Al content coatings experience substantial degradation, which was total for the T22 specimen exposed at 650 °C. This inferior protective behavior was attributed to an initially lower Al content.

CRediT authorship contribution statement

M. Gutiérrez: Methodology, Conceptualization, Investigation, Writing – original draft. **A. Illana:** Investigation, Writing – original draft, Writing – review & editing. **A. Bahillo:** Methodology, Resources. **M.J. Benito:** Methodology, Resources. **G. García-Martín:** Writing – original draft, Writing – review & editing. **F.J. Pérez:** Supervision, Funding acquisition, Writing – review & editing. **A. Agüero:** Conceptualization, Investigation, Resources, Writing – original draft, Writing – review & editing, Supervision.

Declaration of competing interest

The authors declare that they have no known competing financial interests or personal relationships that could have appeared to influence the work reported in this paper.

Data availability

The data that has been used is confidential.

Acknowledgments

This research was funded by EC for financial support within the frame of the Horizon 2020 project BELENUS (G.A. No. 815147) and financially supported by the Ministry of Science and Innovation (GENERA ENE2014- 52359-C3-2-R project). The authors gratefully acknowledge the intellectual efforts of all partners and, also, the technical support from the Research Support Center of X-ray diffraction from Universidad Complutense de Madrid (UCM). During the writing of this scientific contribution, A. Illana was supported by a Margarita Salas grant (CT31/21) by the UCM; within the Multi-year call for the requalification of the Spanish University System for 2021-2023, financed by the Ministry of Universities with funds from Next Generation from the European Union.

References

[1] L. Armesto, A. Bahillo, A. Cabanillas, K. Veijonen, J. Oter, Co-combustion of coal and olive oil industry residues in fluidised bed, Fuel 82 (8) (2003) 993–1000.
[2] M. Ni, D. Leung, M. Leung, K. Sumathy, An overview of hydrogen production from biomass, Fuel Process. Technol. 87 (5) (2006) 461–472.
[3] E. T. S. A. P. a. I. R. E. Agency, Biomass Co-firing in Coal Power Plants, 2013.
[4] Y. Xu, K. Yang, J. Zhou, G. Zhao, Coal-biomass co-firing power generation technology: current status, challenges and policy implications, Sustainability 12 (2020) 3692.
[5] I. N. Laboratory, Logistics, Costs, and GHG Impacts of Utility-Scale Cofiring with 20% Biomass, U.S. Department of Energy Bioenergy Technologies Office, 2013.
[6] D. García-Galindo, F. Royo, F. Sebastián, Assessment of biomass co-firing potentials in coal power plants, Strojarstvo 52 (2010) 411–427.
[7] M. Montgomery, S. Jensen, U. Borg, O. Biede, T. Vilhelmsen, Experiences with high temperature corrosion at straw-firing power plants in Denmark, Mater. Corros. 62 (7) (2011) 593–605.
[8] Mercados Eléctricos, ENERGÍA DE LA BIOMASA. http://hrudnick.sitios.ing.uc.cl/alumno12/costosernc/D._Biomasa.html, 2012.
[9] J. Pettersson, J. Svensson, L. Johansson, KCl-induced corrosion of a 304-type austenitic stainless steel in O and in O + H O environment: the influence of temperature, Oxid. Met. 72 (2009) 159–177.
[10] P. Tchoffor, K. Davidsson, H. Thunman, Transformation and release of potassium, chlorine, and sulfur from wheat straw under conditions relevant to dual fluidized bed gasification, Energy Fuel 27 (12) (2013) 7510–7520.
[11] E. Sadeghi, N. Markocsan, S. Joshi, Advances in corrosion-resistant thermal spray coatings for renewable energy power plants. Part I: effect of composition and microstructure, J. Therm. Spray Technol. 28 (2019) 1749–1788.
[12] E. Vakkilainen, Steam Generation from Biomass: Construction and Design of Large Boilers, Butterworth-Heinemann, 2017.
[13] I. Rodilla, M. Contreras, A. Bahillo, Thermogravimetric and mass spectrometric (TG-MS) analysis of subbituminous coal-energy crops blends in N2, air and CO2/O2 atmospheres, Fuel 215 (2018) 506–514.
[14] F. Wu, M. Argyle, P. Dellenback, F. Maohong, Progress in O2 separation for oxy-fuel combustion–a promising way for cost-effective CO2 capture: a review, Prog. Energy Combust. Sci. 67 (2018) 188–205.
[15] J. Adamiec, High temperature corrosion of power boiler components cladded with nickel alloys, Mater. Charact. 60 (10) (2009) 1093–1099.
[16] A. Agüero, I. Baráibar, M. Gutiérrez, M. Hernández, R. Muelas, S. Rodríguez, Biomass corrosion behavior of steels and coatings in contact with KCl/K2SO4 at 550 °C under an oxy-fuel combustion atmosphere: a screening laboratory at 550 °C under an oxy-fuel combustion atmosphere: a screening laboratory, Surf. Coat. Technol. 350 (2018) 188–200.

[17] A. Agüero, V. González, R. Muelas, Diffusion stable aluminide coatings: behaviour under steam and oxy-fuel fire-side conditions at 650 °C and accelerated diffusion tests at 900 °C, Surf. Coat. Technol. 350 (2018) 119–127.
[18] Y. Kawahara, An overview on corrosion-resistant coating technologies in biomass/waste-to-energy plants in recent decades, Coatings 34 (6) (2016).
[19] A. Agüero, Progress in the development of coatings for protection of new generation steam plant components, Energy Mater. 3 (2008) 35–44.
[20] B. Song, K. Voisey, T. Hussain, High temperature chlorine-induced corrosion of Ni50Cr coating: HVOLF, HVOGF, cold spray and laser cladding, Surf. Coat. Technol. 337 (2018) 357–369.
[21] N. Abu-warda, A. López, F. Pedraza, M. Utrilla, Fireside corrosion on T24 steel pipes and HVOF NiCr coatings exposed to different salt mixtures, Corros. Sci. 173 (2020), 108747.
[22] A. Agüero, I. Baraibar, V. González, R. Muelas, D. Plana, Corrosion resistance of novel coatings on ferritic steels for oxycombustion–supercritical steam boilers: preliminary results, Oxid. Met. 85 (2016) 263–281.
[23] S. Stultz, J. Kitto, Steam: Its Generation and Use, The Babcock & Wilcox Company, Barberton, Ohio, EE.UU, 2005.
[24] V. Viswanathan, R. Purgert, P. Rawls, Coal-fired power materials part II, Advanced 166 (9) (2008) 47–49.
[25] D. Zhang, Ultra-supercritical Coal Power Plants: Materials, Technologies and Optimisation, Woodhead Publishing Limited, Sawston, Reino Unido, 2013.
[26] A. Agüero, M. Gutiérrez, V. González, Deposition process of steam resistant slurry coatings for new generation high temperature supercritical steam plants, Mater. High Temp. 27 (2008) 257–265.
[27] A. Agüero, R. Muelas, Steam oxidation of slurry aluminide coatings on ferritic steels for advanced coal-fired steam power plants, in: de 6th International Symposium on High Temperature Corrosion and Protection of Materials, Les Embiez, 2004.
[28] A. Agüero, P. Audigié, S. Rodríguez, V. Encinas-Sánchez, M. de Miguel, F. Pérez, Protective coatings for high temperature molten salt heat storage systems in solar concentration power plants, AIP Conf. Proc. 2033 (2018), 090001.
[29] A. Agüero, M. Gutiérrez, R. Muelas, D. Plana, A. Román, M. Hernández, Laboratory corrosion testing of coatings and substrates simulating coal combustion under a low NOx burner atmosphere, Mater. Corros. 65 (2) (2014) 149–160.
[30] P. Audigié, V. Encinas-Sánchez, S. Rodríguez, F. Pérez, A. Agüero, High temperature corrosion beneath carbonate melts of aluminide coatings for CSP application, Sol. Energy Mater. Sol. Cells 210 (2020), 110514.
[31] K. Chandra, A. Kranzmann, R. Saliwan Neumann, G. Oder, F. Rizzo, High temperature oxidation behavior of 9–12 % Cr ferritic/martensitic steels in a simulated dry oxyfuel environment, Oxid. Met. 83 (3–4) (2015) 291–316.
[32] Y. Niu, H. Tan, S. Hui, Ash-related issues during biomass combustion: alkali-induced slagging, silicate melt-induced slagging (ash fusion), agglomeration, corrosion, ash utilization, and related countermeasures, Prog. Energy Combust. Sci. 52 (2016) 1–61.
[33] H. Ma, C. Zhou, L. Wang, High temperature corrosion of pure Fe, Cr and Fe–Cr binary alloys in O2 containing trace KCl vapour at 750 °C, Corros. Sci. 51 (8) (2009) 1861–1867.
[34] S. Saunders, M. Monteiro, F. Rizzo, The oxidation behaviour of metals and alloys at high temperatures in atmospheres containing water vapour: a review, Prog. Mater. Sci. 53 (2) (2008) 775–837.
[35] T. Dudziak, T. Hussain, N. Simms, High-temperature performance of ferritic steels in fireside corrosion regimes: temperature and deposits, J. Mater. Eng. Perform. 26 (2017) 84–93.
[36] J. Tomeczek, Corrosion modelling of austenitic steel in molten sulphate deposit, Corros. Sci. 49 (4) (2007) 1862–1868.
[37] Z. Zeng, K. Natesan, Z. Cai, D. Gosztola, Effects of chlorine in ash on the corrosion performance of Ni-based alloys in a simulated oxy-fuel environment, Energy Fuels 32 (10) (2018) 10502–10512.
[38] V. Vokál, V. Rohr, M. Pomeroy, M. Schütze, Corrosion of alloys and their diffusion aluminide coatings by KCl:K2SO4 deposits at 650 °C in air, Mater. Corros. 59 (5) (2008) 374–379.
[39] B. Grégoire, C. Oskay, T. Meißner, M. Galetz, Corrosion performance of slurry aluminide coatings in molten NaCl–KCl, Sol. Energy Mater. Sol. Cells 223 (2021), 110974.
[40] S. Kiamehr, T. Lomholt, K. Dahl, T. Christiansen, M. Somers, Application of aluminum diffusion coatings to mitigate the KCl-induced high-temperature corrosion, Mater. Corros. 68 (1) (2016) 82–94.
[41] M. Aho, P. Yrjas, R. Taipale, M. Hupa, J. Silvennoinen, Reduction of superheater corrosion by co-firing risky biomass with sewage sludge, Fuel 89 (9) (2010) 2376–2386.
[42] M. Oksa, T. Varis, K. Ruusuvuori, Performance testing of iron based thermally sprayed HVOF coatings in a biomass-fired fluidised bed boiler, Surf. Coat. Technol. 251 (2014) 191–200.